Wave Propagation in 3-D Spherical Sections by the Chebyshev Spectral Method

Heiner Igel, Institute of Theoretical Geophysics
Department of Earth Sciences
Cambridge, UK

February 11, 1998

Abstract

The elastic wave equation in spherical coordinates is solved on a spherical section by a Chebyshev spectral method. In the presented algorithm the singularities in the governing equations are avoided by centering the physical domain around the equator. The highly accurate pseudo-spectral (PS) derivative operators reduce the required grid size compared to finite-difference (FD) algorithms. The non-staggered grid scheme allows easy extension to general material anisotropy without the additional interpolations required in staggered FD schemes. The boundary conditions previously derived for curvi-linear coordinate systems can directly be applied to the velocity vector and stress tensor in the spherical basis. Such techniques will be important to model the full 3-D characteristics of upper mantle structure and to provide accurate reference solutions for 3-D global models.

Keywords: seismic modelling, synthetic seismograms, wave propagation, spherical Earth, subduction zones, pseudospectral methods.

Submitted to *Geophysical Journal International*

1 Introduction

Understanding the global structure and geodynamical features of the mantle is one of the most important goals in seismology today. To understand the mass flux into and out of the mantle requires a detailed knowledge of the structure

of subduction zones, hot spots, upper mantle discontinuities, etc. Much of the current imaging and modelling of 3-D mantle structure is undertaken using ray-based approximations or long-period seismograms involving other (linearised) approximations. These approximations are not valid when the wavelengths of the propagating wavefield are of the same order as the structures of interest. In such cases it is important to consider scattering effects, which may contain valuable information. Modern high-quality broad-band recordings contain information which is currently not accounted for by essentially ray-based modelling algorithms. Therefore the development of forward modelling tools which simulate a 3-D Earth with high enough frequencies is an important step towards solving some of the current geodynamical problems.

In the past decade discrete grid methods have been widely used in the field of seismic wave propagation. Early algorithms (e.g. Virieux, 1984, 1985) solved the equations in two dimensions using low-order approximations to the space and time derivatives. Later those algorithms were extended to higher orders (e.g. Levander, 1988), to 3-D (e.g. Mora, 1989) and to the general anisotropic case (e.g. Igel, Mora, and Riollet, 1995; Tessmer, 1995).

An alternative to the *local* derivative operators of FD schemes is provided by pseudo-spectral (PS) techniques. PS methods have been widely used in numerical algorithms for wave propagation, computational fluid dynamics and in other fields. For fundamentals on pseudospectral methods the reader is referred to the excellent book by Fornberg (1996). Previous applications to wave propagation problems can be found in Kosloff et al. (1990), Kosloff and Tal-Ezer (1993), Carcione and Wang (1993), Carcione (1994), Tessmer and Kosloff (1994), Tessmer (1995), Komatitsch, Coutel, and Mora (1997).

In PS techniques the space-dependent fields are expanded in a set of orthogonal basis functions which are known *exactly* at a discrete set of points. For example, these basis functions can be Fourier series (regular grid) or Chebyshev polynomials (non-uniform grid defined between [-1,1] with denser grid at the boundaries). The PS techniques have the advantage that the space derivatives can be calculated with high numerical precision. The Chebyshev method furthermore allows an implementation of boundary conditions (e.g. traction-free, or non-reflecting) with the same accuracy as within the medium. This is a problem with the FD method, where boundary conditions are usually implemented with lower accuracy than inside the medium. The drawback of the PS technique is that due to the length of the derivative operator more numerical operations are needed. However, the overall performance of FD and PS methods - assuming the same accuracy - are similar, depending mostly on hardware.

One major advantage of the PS technique is in connection with anisotropy. While staggered grids are to be preferred in FD algorithms, they are not required with the PS technique. Since staggering requires that elements of stress, strain, and stiffness tensor to be defined at different locations, Hooke's law forces (numerical) interpolations to be carried out in the general case, degrading the overall accuracy (Igel et al., 1995).

In this paper we propose a solution to the elastic anisotropic wave equation for spherical sections using the Chebyshev method. This can be seen as a special case of the more general formulation by Carcione (1995) for generalised coordinates. However, the direct implementation of the wave equation in spherical coordinates is far more convenient than in a cartesian frame. Furthermore, it will allow the addition of small perturbations to the spherical grid (e.g. ellipticity, surface topography, topography of internal boundaries) by defining appropriate stretching functions.

2 The Wave Equation

Following the approach of previous authors (e.g. Virieux, 1986; Carcione, 1994; Tessmer, and Kosloff, 1994; Tessmer, 1995) we write the governing equations as a first order system. We denote by σ_{ij} and v_i the elements of the stress tensor and velocity vector, respectively. In general form the equations of motion are

$$\begin{aligned} \partial_t v_i &= \nabla_j(\sigma_{ij} + M_{ij}) + f_i \\ \partial_t \sigma_{ij} &= c_{ij\,kl}\partial_t \epsilon_{kl} \quad , \end{aligned} \tag{1}$$

where $c_{ij\,kl}$ are the elements of the stiffness tensor and M_{ij} are the elements of the source moment tensor, f_i being volumetric forces.

In spherical coordinates $[r, \theta, \varphi]$ these equations (time and space dependence implicit) take the form (e.g. Lapwood and Usami, 1981, p. 28 and p.78)

$$\begin{aligned} \rho\partial_t v_r &= \partial_r \sigma_{rr} + \frac{1}{r}\partial_\theta \sigma_{r\theta} + \frac{1}{r\sin\theta}\partial_\varphi \sigma_{r\varphi} \\ &\quad + \frac{1}{r}(2\sigma_{rr} - \sigma_{\theta\theta} - \sigma_{\varphi\varphi} + \sigma_{r\theta}\cot\theta) + f_r \\ \rho\partial_t v_\theta &= \partial_r \sigma_{r\theta} + \frac{1}{r}\partial_\theta \sigma_{\theta\theta} + \frac{1}{r\sin\theta}\partial_\varphi \sigma_{\theta\varphi} \\ &\quad + \frac{1}{r}((\sigma_{\theta\theta} - \sigma_{\varphi\varphi})\cot\theta + 3\sigma_{r\theta}) + f_\theta \\ \rho\partial_t v_\varphi &= \partial_r \sigma_{r\varphi} + \frac{1}{r}\partial_\theta \sigma_{\theta\varphi} + \frac{1}{r\sin\theta}\partial_\varphi \sigma_{\varphi\varphi} \\ &\quad + \frac{1}{r}((3\sigma_{r\varphi} + 2\sigma_{\theta\varphi}\cot\theta)) + f_\varphi \end{aligned} \tag{2}$$

where the elements ϵ_{ij} of the strain tensor are given by

$$\begin{aligned} \partial_t \epsilon_{rr} &= \partial_r v_r \\ \partial_t \epsilon_{\theta\theta} &= \frac{1}{r}\partial_\theta v_\theta + \frac{1}{r}v_r \end{aligned}$$

$$
\begin{aligned}
\partial_t \epsilon_{\varphi\varphi} &= \frac{1}{r\sin\theta}\partial_\varphi v_\varphi + \frac{1}{r} v_r + \frac{\cot\theta}{r} v_\theta \\
\partial_t \epsilon_{r\theta} &= \frac{1}{2}(\frac{1}{r}\partial_\theta v_r + \partial_r v_\theta - \frac{1}{r} v_\theta) \\
\partial_t \epsilon_{\theta\varphi} &= \frac{1}{2}(\frac{1}{r\sin\theta}\partial_\varphi v_\theta + \frac{1}{r}\partial_\theta v_\varphi - \frac{\cot\theta}{r} v_\varphi) \\
\partial_t \epsilon_{r\varphi} &= \frac{1}{2}(\frac{1}{r\sin\theta}\partial_\varphi v_r + \partial_r v_\varphi - \frac{1}{r} v_\varphi) \ . \qquad (3)
\end{aligned}
$$

In the isotropic case, the stress-strain relation is

$$
\begin{aligned}
\sigma_{rr} &= \lambda\Delta + 2\mu\epsilon_{rr} + M_{rr} \\
\sigma_{\theta\theta} &= \lambda\Delta + 2\mu\epsilon_{\theta\theta} + M_{\theta\theta} \\
\sigma_{\varphi\varphi} &= \lambda\Delta + 2\mu\epsilon_{\varphi\varphi} + M_{\varphi\varphi} \\
\sigma_{r\theta} &= 2\mu\epsilon_{r\theta} + M_{r\theta} \\
\sigma_{\theta\varphi} &= 2\mu\epsilon_{\theta\varphi} + M_{\theta\varphi} \\
\sigma_{r\varphi} &= 2\mu\epsilon_{r\varphi} + M_{r\varphi} \quad , \qquad (4)
\end{aligned}
$$

where λ and μ are the Lamé parameters and $\Delta = \epsilon_{rr} + \epsilon_{\theta\theta} + \epsilon_{\varphi\varphi}$.

In the following section we describe the numerical solution to these equations.

3 The Numerical Algorithm

3.1 Physical and Computational Domain

To solve the equations described in the previous sections, all space-dependent fields are defined on a curved grid, a spherical section, as illustrated in Figure 1. In each dimension j, the fields are defined on the Chebyshev collocation points $x_i^j = \cos(i\pi/N^j), i = 0, ..., N^j$, where N^j+1 is the total number of grid points along dimension j. This non-uniform discretization leads to decreasing grid spacing at the boundaries. Since, by the stability criterion, this requires unreasonably small time steps, stretching is applied in all dimensions to improve the performance of the algorithm. Such stretching functions are described in Kosloff et al. (1990), Kosloff and Tal-Ezer (1993), and Carcione and Wang (1993). It allows time steps of order $O(N^{-1})$ rather than $O(N^{-2})$ in the original Chebyshev discretization.

The singularities in the governing equations are avoided by centering the spherical section around $\theta = \pi/2$. Clearly, the effective grid spacing becomes smaller with decreasing r. The depth extent of the model should be carefully designed for the particular application to avoid time increments which are too small.

3.2 Space Derivatives and Time Extrapolation

In all spatial dimensions the derivatives are evaluated with the Chebyshev derivative operator (e.g. Fornberg, 1996). The derivatives can be evaluated either by matrix-matrix multiplication (MMM) or the Fast-Fourier Transform (FFT). In the three-dimensional case the number of grid points per axis is rather small (e.g. < 200). We find that in this case the MMM outperforms the FFT, which is in accordance with the results reported by Fornberg (1996).

The time extrapolation is carried out by a fourth-order Runge-Kutta method. An algorithm similar to the one described in this paper - for the two-dimensional cartesian case - is described in Carcione and Wang (1993).

3.3 Boundary Conditions

Since we are modelling only a section of the sphere we want to omit reflections from the sides of our physical domain except the outer surface. The great advantage of the Chebyshev method in comparison to low or high-order finite-difference methods is the implementation of absorbing and free-surface boundary conditions with spectral accuracy.

Boundary conditions for the Chebyshev method have previously been derived using the concept of characteristic variables (Gottlieb, Gunzburger, and Turkel, 1982). A discussion on the derivation of these boundary conditions can be found in Carcione and Wang (1993), Carcione (1994), and for the general anisotropic case in Tessmer (1995). In curvi-linear coordinates the vectors and tensors have to be rotated into a system normal to the particular boundary. Clearly, we are already using the rotated fields and can therefore directly apply the boundary conditions originally derived from the cartesian equations by a one-dimensional analysis.

For example, the free surface condition at $r = 6371$km requires that $\sigma_{rr} = \sigma_{r\theta} = \sigma_{r\varphi} = 0$. Denoting the corrected boundary values by superscript ^{new}, this condition can be satisfied by

$$
\begin{aligned}
v_\theta^{\text{new}} &= v_\theta^{\text{old}} - \frac{1}{\sqrt{\rho\mu}}\,\sigma_{r\theta}^{\text{old}} \\
v_\varphi^{\text{new}} &= v_\varphi^{\text{old}} - \frac{1}{\sqrt{\rho\mu}}\,\sigma_{r\varphi}^{\text{old}} \\
v_r^{\text{new}} &= v_r^{\text{old}} - \frac{1}{\sqrt{\rho(\lambda+2\mu)}}\,\sigma_{rr}^{\text{old}} \\
\sigma_{\theta\theta}^{\text{new}} &= \sigma_{\theta\theta}^{\text{old}} - \frac{\lambda}{\lambda+2\mu}\,\sigma_{rr}^{\text{old}} \\
\sigma_{\varphi\varphi}^{\text{new}} &= \sigma_{\varphi\varphi}^{\text{old}} - \frac{\lambda}{\lambda+2\mu}\,\sigma_{rr}^{\text{old}}
\end{aligned}
\tag{5}
$$

where the superscript ^{old} denotes the values obtained after applying the operators within the medium. The only variable which remains unchanged is $\sigma_{r\varphi}$.

At the bottom and all the side boundaries we apply non-reflecting boundary conditions. Using the same notation as above, the condition at the bottom boundary at $r = r_{min}$ reads

$$
\begin{aligned}
v_\theta^{\text{new}} &= \frac{1}{2}(v_\theta^{\text{old}} + \frac{1}{\sqrt{\rho\mu}}\ \sigma_{r\theta}^{\text{old}}) \\
v_\varphi^{\text{new}} &= \frac{1}{2}(v_\varphi^{\text{old}} + \frac{1}{\sqrt{\rho\mu}}\ \sigma_{r\varphi}^{\text{old}}) \\
v_r^{\text{new}} &= \frac{1}{2}(v_r^{\text{old}} + \frac{1}{\sqrt{\rho(\lambda+2\mu)}}\ \sigma_{rr}^{\text{old}} \\
\sigma_{\theta\theta}^{\text{new}} &= \sigma_{\theta\theta}^{\text{old}} - \frac{\lambda}{2(\lambda+2\mu)}\ (\sigma_{rr}^{\text{old}} - \sqrt{\rho(\lambda+2\mu)}\ v_r^{\text{old}}) \\
\sigma_{\varphi\varphi}^{\text{new}} &= \sigma_{\varphi\varphi}^{\text{old}} - \frac{\lambda}{2(\lambda+2\mu)}\ (\sigma_{rr}^{\text{old}} - \sqrt{\rho(\lambda+2\mu)}\ v_r^{\text{old}}) \\
\sigma_{rr}^{\text{new}} &= \frac{1}{2}(\sigma_{rr}^{\text{old}} + \sqrt{\rho(\lambda+2\mu)}\ v_r^{\text{old}}) \\
\sigma_{r\theta}^{\text{new}} &= \frac{1}{2}(\sigma_{r\theta}^{\text{old}} + \frac{1}{\sqrt{\rho\mu}}\ v_\theta^{\text{old}}) \\
\sigma_{r\varphi}^{\text{new}} &= \frac{1}{2}(\sigma_{r\varphi}^{\text{old}} + \frac{1}{\sqrt{\rho\mu}}\ v_\varphi^{\text{old}})\ \ . \qquad (6)
\end{aligned}
$$

The accuracy of the implementation of the boundary conditions depends on the grid spacing near the boundaries. The stretching functions applied to each dimension have to be carefully designed to avoid inaccuracies near the boundaries. Appropriate parameters are discussed in Carcione and Wang (1993).

4 Numerical Examples

To demonstrate the feasibility of this algorithm we first compare it with a finite-difference (FD) solution and then simulate a dip-slip earthquake in a simplified high-velocity slab geometry.

4.1 Comparison with Finite Differences

To address the accuracy of the presented algorithm we compare seismograms calculated with the PS technique to FD seismograms. The FD seismograms are calculated with the P-SV algorithm for wave propagation in spherical coordinates with rotational symmetry (Igel and Weber, 1996). This code has previously been compared and verified with other solutions within the COSY project (Igel, Geller, and Romanowicz, 1997). The symmetry of the P-SV algorithm

limits the sources to those with rotational symmetry (e.g. explosions or vertical forces). The PS calculations were carried out on a 100x100x100 grid for a 50°x 50°x 3000km section. Seismograms are obtained at arbitrary locations at the surface by interpolating between adjacent grid points. The depth of the explosive source is 600km. To avoid numerical artefacts the source is distributed by a spatial Gauss function with 75km halfwidth. The seismograms are filtered with a cut-off at 15 seconds period. We compare vertical components calculated for an isotropic model (v_p=13km/s, v_s=6.5km/2). Results at epicentral distances between 1°and 25°are shown in Figure 2. There is excellent agreement between FD and PS results. The rms-difference between the two solutions calculated in a window of two dominant periods is less than 0.1%.

4.2 Slab Simulation Parameters

For the slab simulation the spherical section is defined on a 80x80x50 grid (longitude, latitude, depth, respectively). The physical domain is 80°x 80°wide at the surface and the depth range is 5000km. The angular domain is centered around $\theta = 90°$ and $\varphi = 130°$. Thus at the surface the grid spacing is approximately 100km in each dimension. Towards the bottom boundary the grid spacing decreases to a minimum 10km. 3000 time steps with an increment of 0.25 seconds lead to a total recording time of 750 seconds. The dominant period of the source-time function is 50 seconds.

The background spherically-symmetric model is the isotropic part of PREM (Dziewonski and Anderson, 1981). The high-velocity perturbation is 10°x 4°wide and 700km deep. The velocities and densities are 5% larger inside the slab with respect to PREM.

4.3 Results

Figures 3 shows snapshots of wave propagation at the Earth's surface 550 seconds after the source origin time. The source is a pure dip-slip at 600km depth. Snapshots are shown for the spherically symmetric background model. The effective action of the absorbing boundaries can be seen in the snapshots. The strong azimuthal variation of the wavefield is due to the source radiation pattern.

Wave motion inside the Earth's mantle is shown in Figure 4 in sections of constant φ and θ. In Figure 4, top, the SH part of mantle wave propagation is shown, where motion is confined to the mantle and the wavefield is totally reflected at the core-mantle boundary. The amplitude of the surface reflections is stronger than those of the downward (and subsequently reflected) signals. This is because the smaller velocities near the Earth's surface have caused them to propagate a shorter distance. In Figure 4, bottom, the radial part of the wavefield is shown and both S and P waves can be seen, including a converted P wave propagating inside the outer core.

The seismograms for the spherically symmetric background model PREM are shown in Figure 5 for various velocity components and receiver profiles. The ray-theoretical arrival times of the phases P, sP, and S are indicated. The differential seismograms for the slab model obtained after subtracting the PREM seismograms are shown in Figure 6. The slab mainly affects the waves recorded at small epicentral distances propagating vertically upwards (through the slab). At larger distances the slab seems to affect later arrivals more than the direct waves.

5 Conclusion

We present a numerical algorithm for solving the elastic wave equation in spherical coordinates on a spherical section using the PS method based on Chebyshev polynomials. With the high accuracy of modern broad-band recordings, accurate forward modelling algorithms for 3-D structures will play an important role in understanding and interpreting fine details in the recorded wavefields. The more and more detailed regional seismic velocity images obtained from tomography will soon allow us to focus on dynamic rather than kinematic effects.

The potential of this approach is in its accurate handling of boundary conditions (free surface or absorbing). It will allow us to study full wave effects of 3-D heterogeneous structures (subduction zones, hot spots, lowermost mantle structure (D"), etc.) on various length scales in a spherical system. Furthermore the centered scheme allows modelling of generally anisotropic structures.

Because 3-D algorithms will have to rely on relatively coarse grids for some time, the spherically symmetric background model may not be well represented by an arbitrary discretization in depth. This could be avoided by implementing a multi-domain solution, where the different domains may represent depth sections between major discontinuities. The domains could be connected applying the boundary conditions for discontinuities in welded contact. This is work in progress.

Acknowledgments

I gratefully acknowledge the Enigma Project for High Performance Computing in Geopysics at the Institute of Theoretical Geophysics in Cambridge for access to their computational facilities (DEC 8400-5/625). I particularly thank Jonathan Harris from DEC for his help in parallelising and optimising the algorithm. This work was funded by NERC Grant GR3/10086. Contribution No. XXXX of the Department of Earth Science and Institute of Theoretical Geophysics, University of Cambridge.

References

[1] Carcione, J.M., 1994, The wave equation in generalised coordinates, *Geophysics*, **59**, 1911-1919.

[2] Carcione, J.M. and Wang, J.-P., 1993, A Chebyshev collocation method for the elastodynamic equation in generalised coordinates, *Comp. Fluid. Dyn.*, **2**, 269-290.

[3] Fornberg, B., 1996, A practical guide to pseudospectral methods, *Cambridge University Press.*

[4] Gottlieb, D., Gunzburger, M. and Turkel, E., 1982, On numerical boundary treatment for hyperbolic systems, *SIAM J. Numer. Anal.*, **19**, 671-682.

[5] Igel, H., P. Mora, and Riollet, B., 1995, Anisotropic wave propagation through finite-difference grids, *Geophysics*, **60**, 1203-1216.

[6] Igel, H., and M. Weber, 1996, P-SV wave propagation in the Earth's mantle using finite differences: Application to heterogeneous lowermost mantle structure, *Geop. Res. Let.*, 23, 415-418.

[7] Igel, H., Geller, R., and B. Romanowicz, 1997, The COSY Project: A comparative study of modelling techniques in global seismology, IASPEI Meeting, Thessaloniki, Technical Programme, 356.

[8] Komatitsch, D., Coutel, F. and Mora, P., 1996, Tensorial formulation of the wave equation for modelling curved interfaces, *Geophys. J. Int.*, 127, 156-168.

[9] Kosloff, D., Kessler, D., Filho, A.Q., Tessmer, E., Behlem A., 1990, Solution of the equations of dynamic elasticity by a Chebyshev spectral method, *Geophysics*, **55**, 734-748.

[10] Kosloff, D. and Tal-Ezer, H., 1993, Modified Chebyshev pseudospectral method with $O(N^{-1})$ time step restriction, *J. Comp. Phys.*, **104**, 457-469.

[11] Lapwood, E.R. and Usami, T., 1981, Free oscillations of the Earth, *Cambridge University Press.*

[12] Levander, A.R., 1988, Fourth-order finite-difference P-SV seismograms, *Geophysics*, **53**, 1425-1436.

[13] Mora, P., 1989, Modeling anisotropic seismic waves in 3-D, Expanded abstracts, 59th Annual International Meeting of Exploration Geophysicists, 1039-1043.

[14] Tessmer, E. and Kosloff, D., 1994, 3-D elastic modelling with surface topography by a Chebychev spectral method, *Geophysics*, **59**, 464-473.

[15] Tessmer, E., 1995, 3-D seismic modelling of general material anisotropy in the presence of the free surface by a Chebyshev spectral method, *Geophys. J. Int.*, **121**, 557-575.

[16] Virieux, J., 1984, SH-wave propagation in heterogeneous media: velocity-stress finite-difference method, *Geophysics*, **49**, 1933-1942.

[17] Virieux, J., 1985, P-SV wave propagation in heterogeneous media: velocit-stress finite-difference method, *Geophysics*, **51**, 889-901.

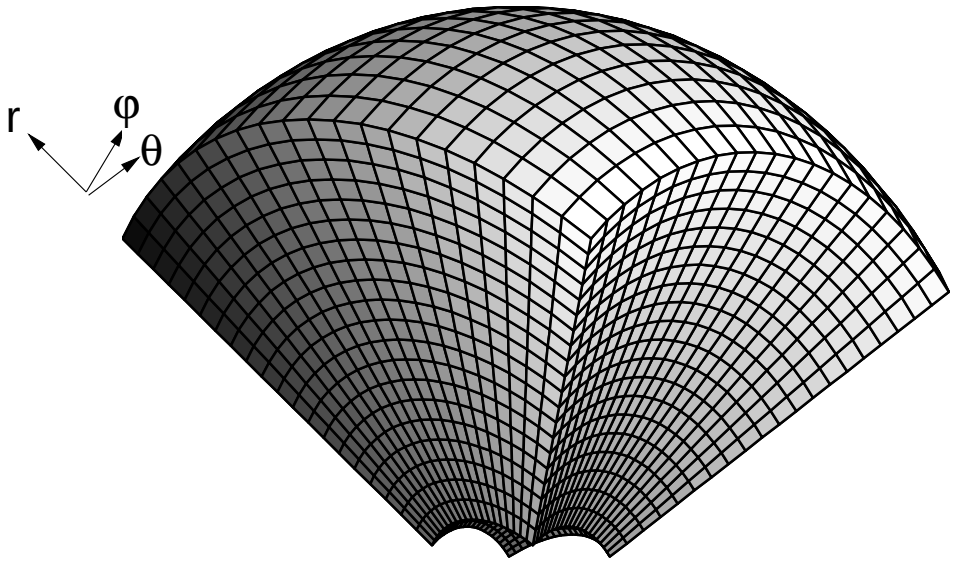

Figure 1: Physical domain for 3-D simulations. The angular range in φ and θ is 80°. The section is centered around the equator. The radial range is 1371km $\leq r \leq$ 6371km.

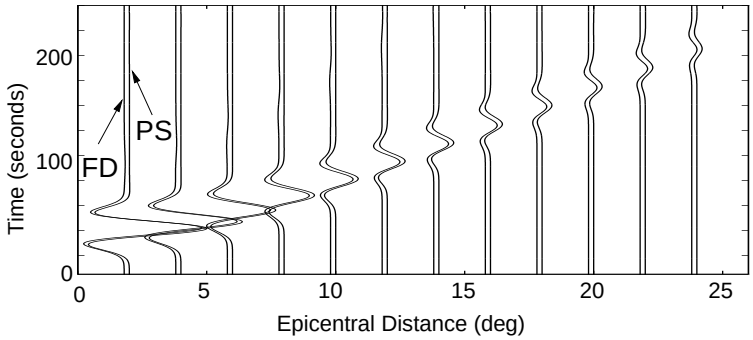

Figure 2: Comparison of radial velocity components calculated with FD (left traces) and with PS (right traces) for an explosion source at 600km depth. The model is isotropic (see text), sampled at an (average) interval of $\approx$30km. The dominant period is $\approx$30 seconds.

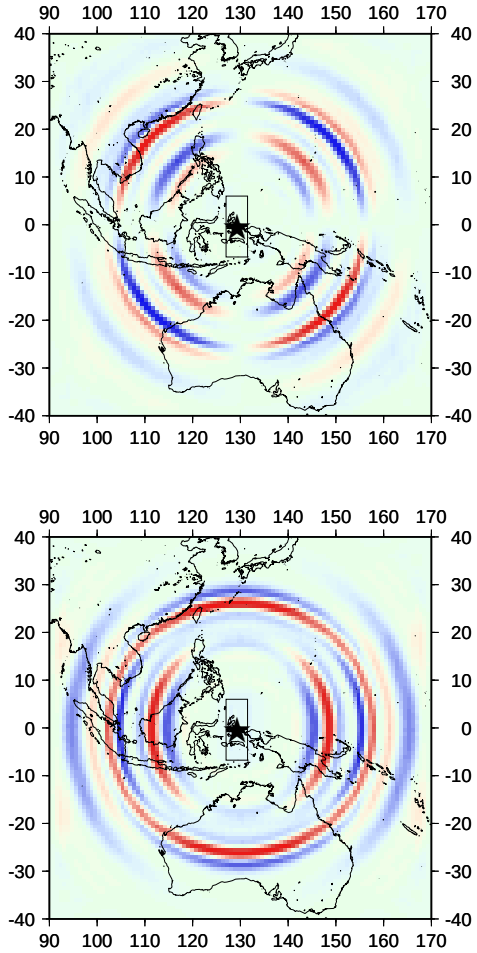

Figure 3: Top: The v_θ component of velocity as observed at the surface for a source at 600km depth. The only non-zero element of M_{ij} is $M_{r\theta} = 1$, corresponding to a pure dip-slip source. Coastlines are added to show the scales involved. The epicenter location is indicated by a star. The high-velocity anomaly below the box ranges to a depth of 700km. Bottom: The v_φ component of velocity at the surface for the same source.

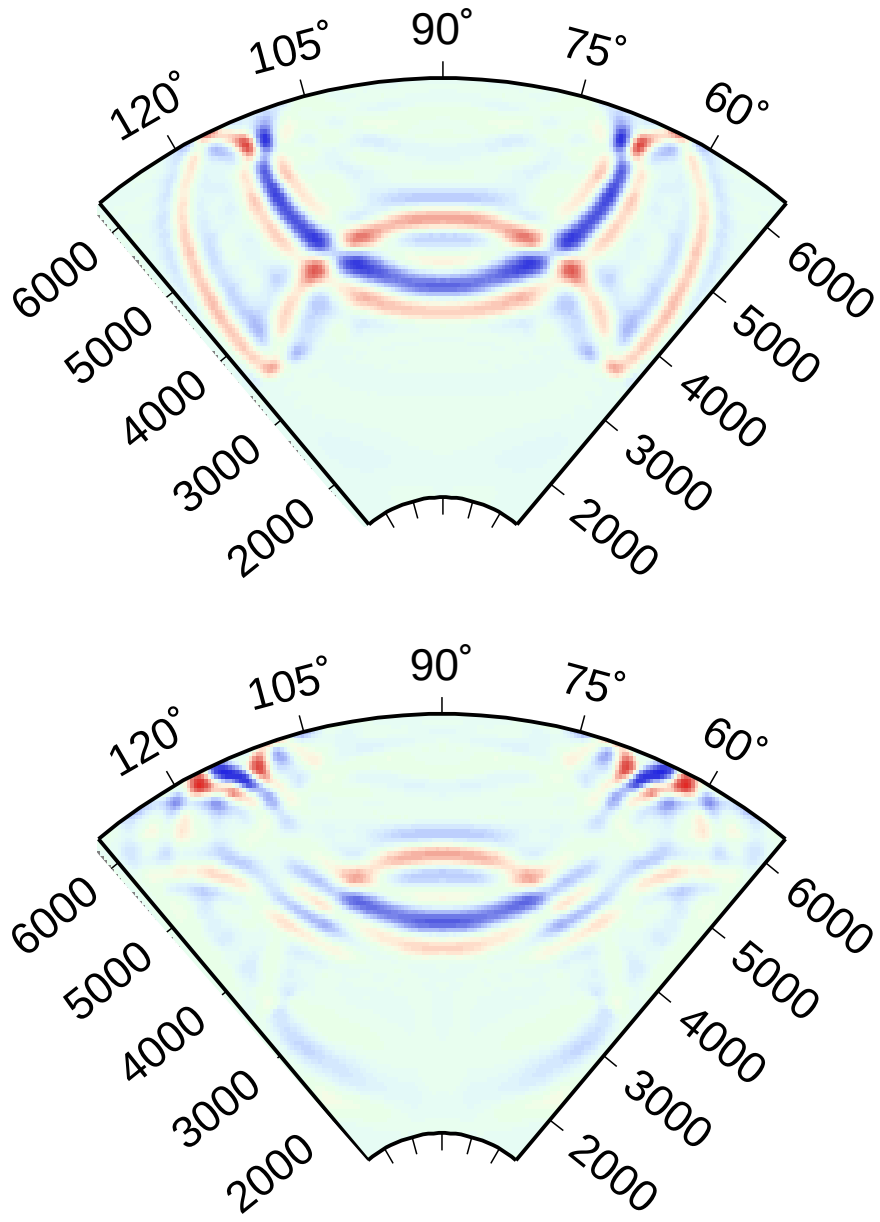

Figure 4: Left: Velocity component v_φ along $\theta = 90°$. This is the SH part of the wavefield. In this plane, motion is confined to the Earth's mantle. Right: Velocity component v_θ along $\varphi = 130°$. A converted P wave can be seen propagating in the outer core. The largest energy is in the developing surface multiples in the upper mantle.

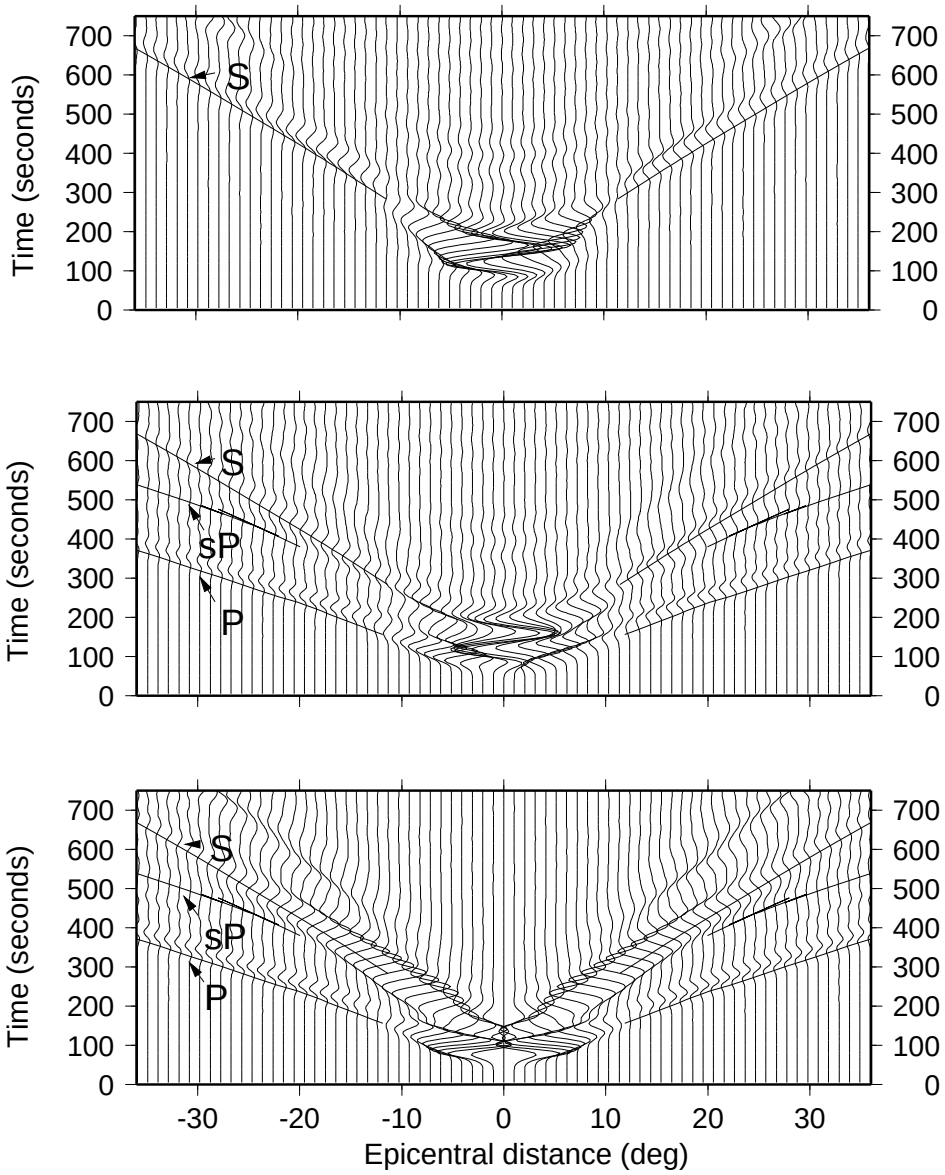

Figure 5: Seismograms for simulations shown in the previous figures. Top: v_φ component recorded along the θ-axis at φ=90°. Middle: v_φ component recorded along the φ-axis at θ=130°. Bottom: v_r component recorded along the φ-axis at θ=130°.

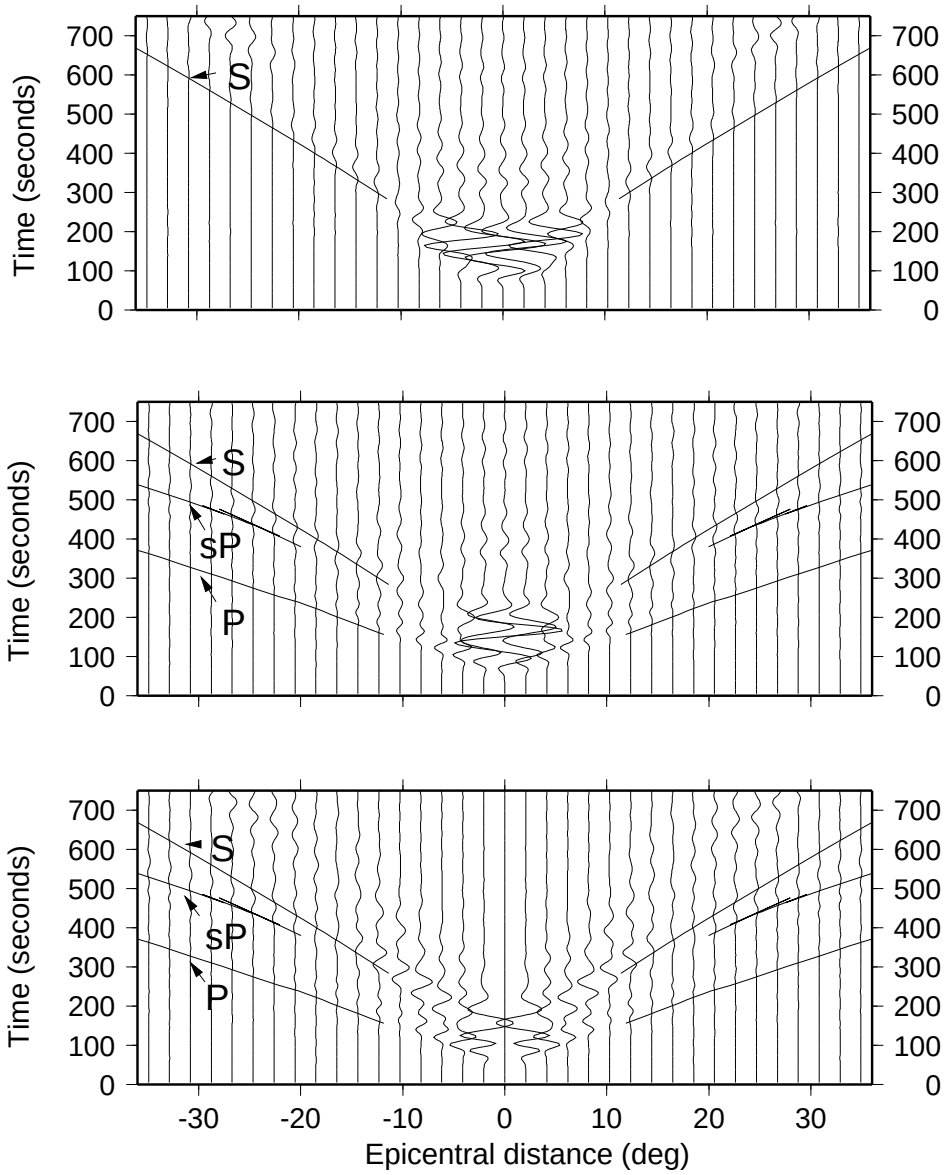

Figure 6: Residuals Seismograms for simulations shown in the previous figures. Top: v_φ component recorded along the θ-axis at φ=90°. Middle: v_φ component recorded along the φ-axis at θ=130°. Bottom: v_r component recorded along the φ-axis at θ=130°.